Supplementary Information of "Characterization and decomposition of the natural van der Waals $SnSb_2Te_4$ under compression"

Juan A. Sans,[a,] Rosario Vilaplana,[b] E. Lora Da Silva,[a] Catalin Popescu,[c] Vanesa P. Cuenca-Gotor,[a] Adrián Andrada-Chacón,[d] Javier Sánchez-Benitez,[d] Oscar Gomis,[b] André L. J. Pereira,[a,e] Plácida Rodríguez-Hernández,[f] Alfonso Muñoz,[f] Dominik Daisenberger,[g] Braulio García-Domene,[h] Alfredo Segura,[h] Daniel Errandonea,[h] Ravhi S. Kumar,[i] Oliver Oeckler,[j] Philipp Urban,[j] Julia Contreras-García,[k] and Francisco J. Manjón[a]*

[a] Instituto de Diseño para la Fabricación y Producción Automatizada, MALTA-Consolider Team, Universitat Politècnica de València, Valencia, Spain
[b] Centro de Tecnologías Físicas, MALTA-Consolider Team, Universitat Politècnica de València, Valencia, Spain
[c] ALBA-CELLS, Barcelona, Spain
[d] Departamento de Química-Física, MALTA-Consolider Team, Universidad Complutense de Madrid, Madrid, Spain
[e] Grupo de Pesquisa de Materiais Fotonicos e Energia Renovavel - MaFER, Universidade Federal da Grande Dourados, Dourados, MS 79825-070, Brazil
[f] Departamento de Física, MALTA-Consolider Team, Instituto de Materiales y Nanotecnología, Universidad de La Laguna, Tenerife, Spain
[g] Diamond Light Source Ltd, Oxon, England
[h] Departamento de Física Aplicada-ICMUV, MALTA-Consolider Team, Universidad de Valencia, Valencia, Spain
[i] Department of Physics, University of Illinois at Chicago, Chicago IL 60607-7059, USA
[j] Institut für Mineralogie, Kristallographie und Materialwissenschaft, Universität Leipzig, Germany
[k] CNRS, UMR 7616, Laboratoire de Chimie Théorique, F-75005, Paris, France

*Corresponding author: juasant2@upv.es

Structural features of $SnSb_2Te_4$

In $SnSb_2Te_4$, roughly 50% of Sb cations are mixed with Sn cations in the 3a Wyckoff site and 25% of Sn are mixed with Sb cations in 6c atomic position. This result will not affect to the interlayer character featured by van der Waals interactions between Te sublayers. The similar covalent radii of Sn and Sb (1.39 Å in both) **[S1]** and ionic radii in an octahedral distribution, with a value of 83 Å for Sn and 90 Å for Sb **[S2]** suggests that the perturbation in the Sb-Te and Sn-Te octahedral units will be mostly influence by the electronic interactions, instead of geometrical effects. On the other hand, the isostructural $SnBi_2Te_4$ shows a similar mixed cationic occupancy as its counterpart $SnSb_2Te_4$. According to Kuropatawa and Kleinke,**[S3]** Sn remains mostly on the 3a atomic position with an occupancy of 74% like Bi that is in 6c atomic position with an occupancy of 68%.

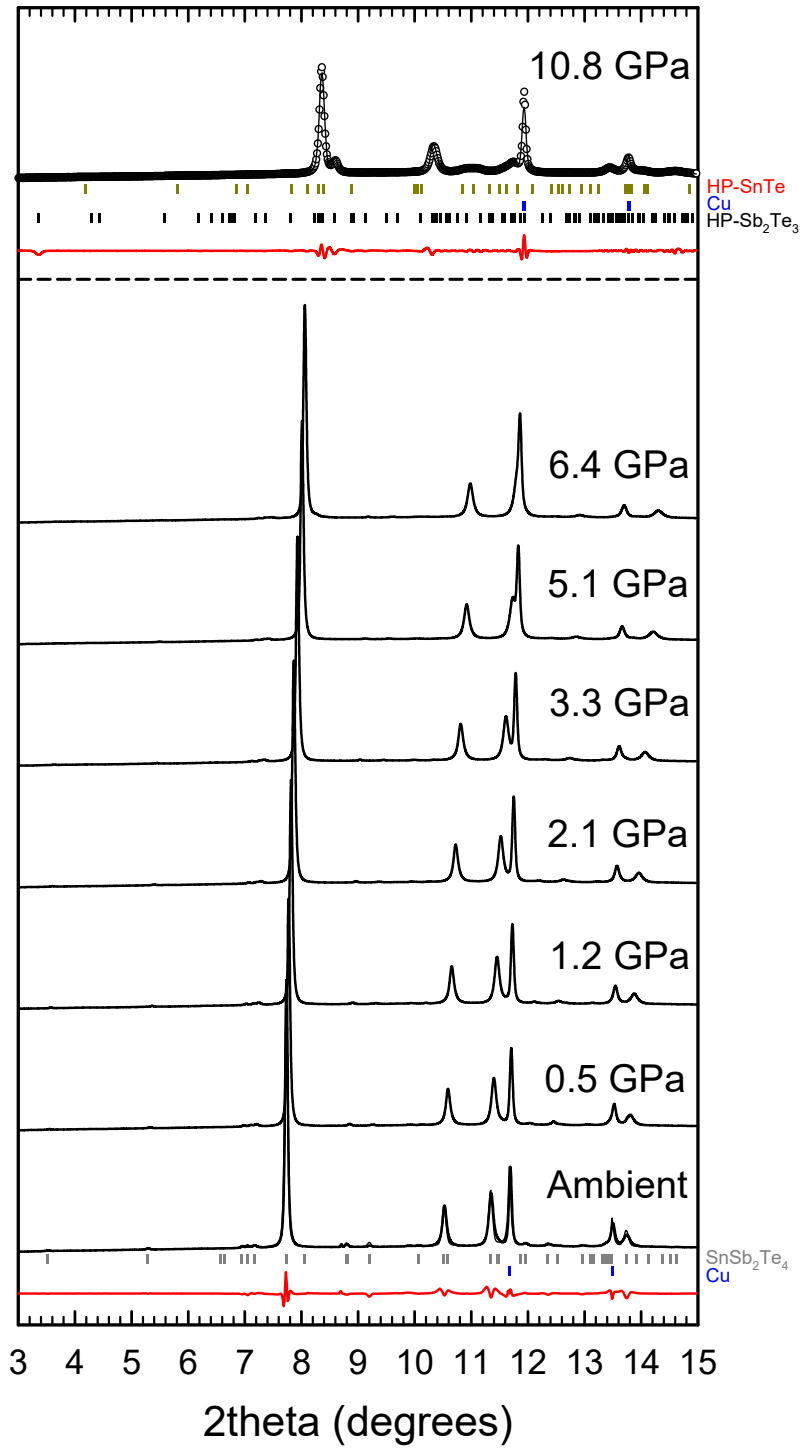

Figure S1. HP-ADXRD patterns of $SnSb_2Te_4$ at room temperature up to 11 GPa.

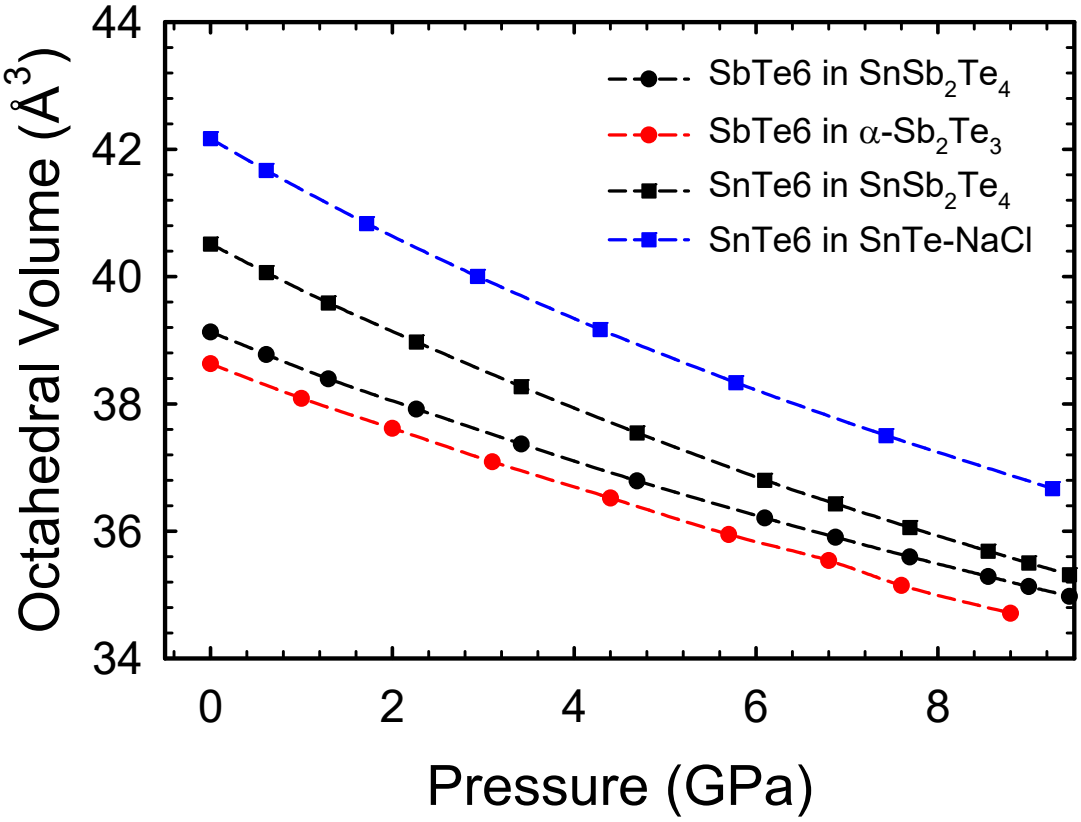

Figure S2. Pressure dependence of the theoretical volumes of $SbTe_6$ and $SnTe_6$ octahedra in $SnSb_2Te_4$ and in α-Sb_2Te_3 **[S4]** and cubic SnTe **[S5]**.

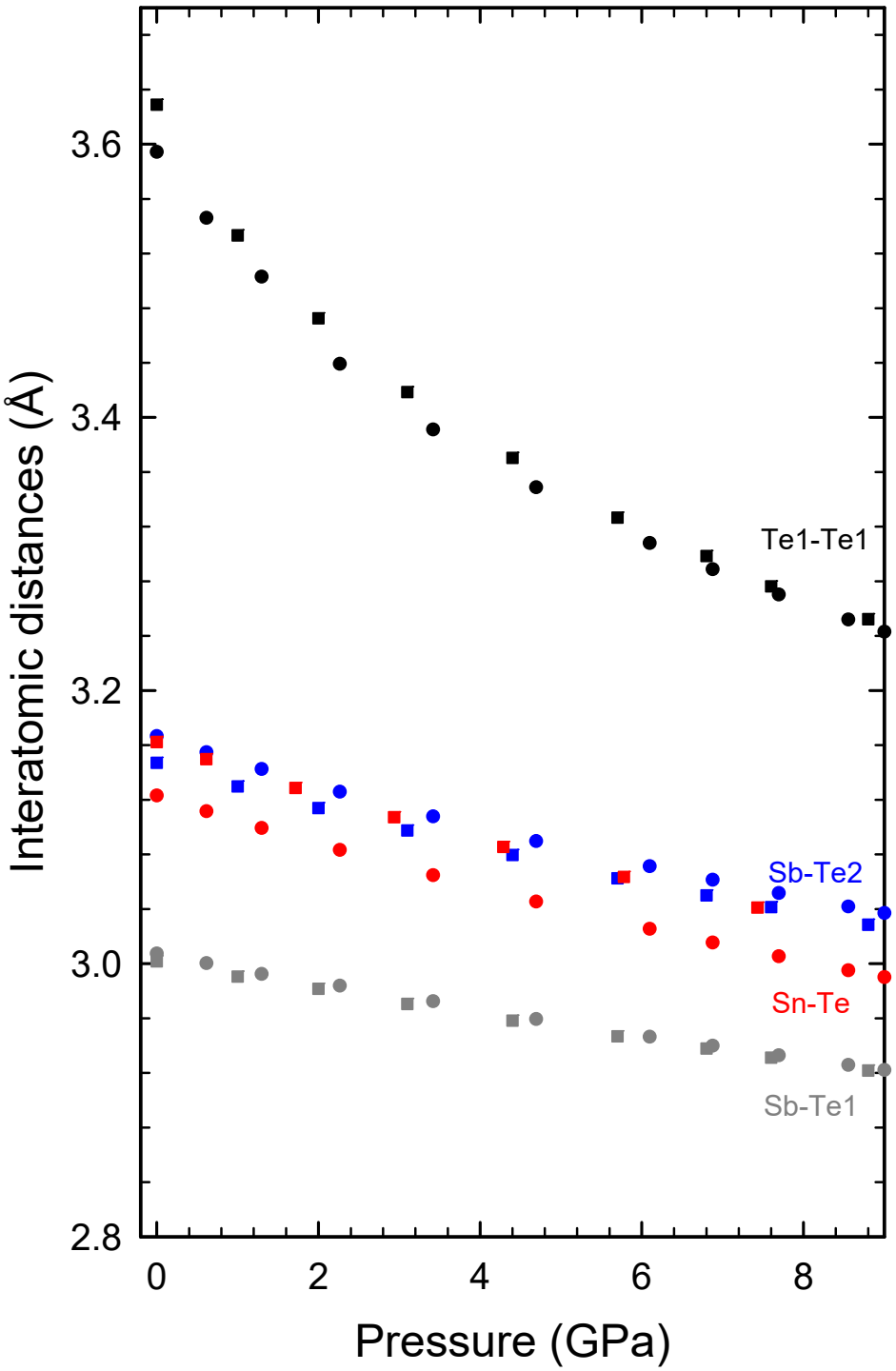

Figure S3. Pressure dependence of the theoretical interatomic distances in $SnSb_2Te_4$ (circles) and its binary constituents (squares), α-Sb_2Te_3 (blue, grey and black) and c-SnTe (red).

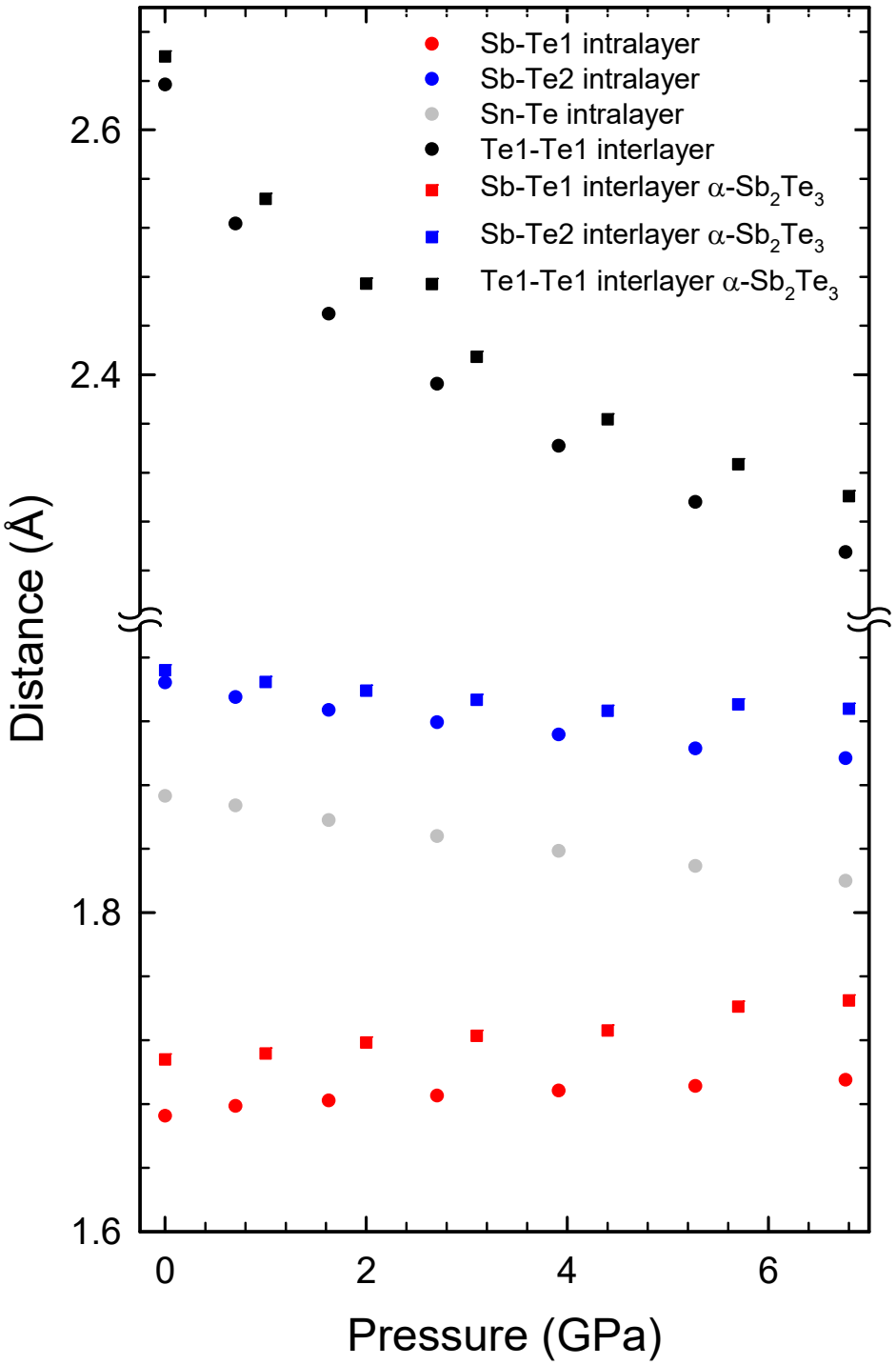

Figure S4. Pressure dependence of the theoretical interplanar distances: Te1-Te1 interlayer distance and the different intralayer distances in $SnSb_2Te_4$ (circles), and in α-Sb_2Te_3 and c-SnTe (squares).

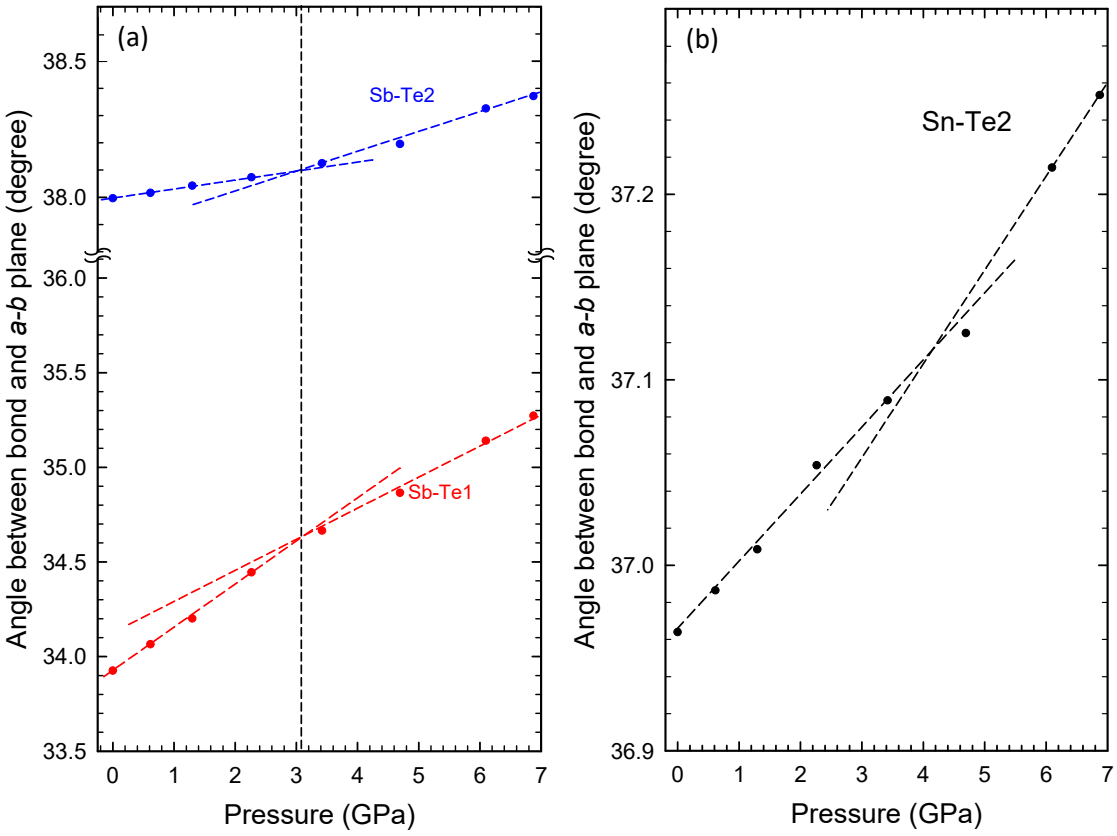

Figure S5. Pressure dependence of the theoretical angle between the *ab*-plane and the Sb-Te1 and Sb-Te2 (a) and Sn-Te (b) bonds in $SnSb_2Te_4$.

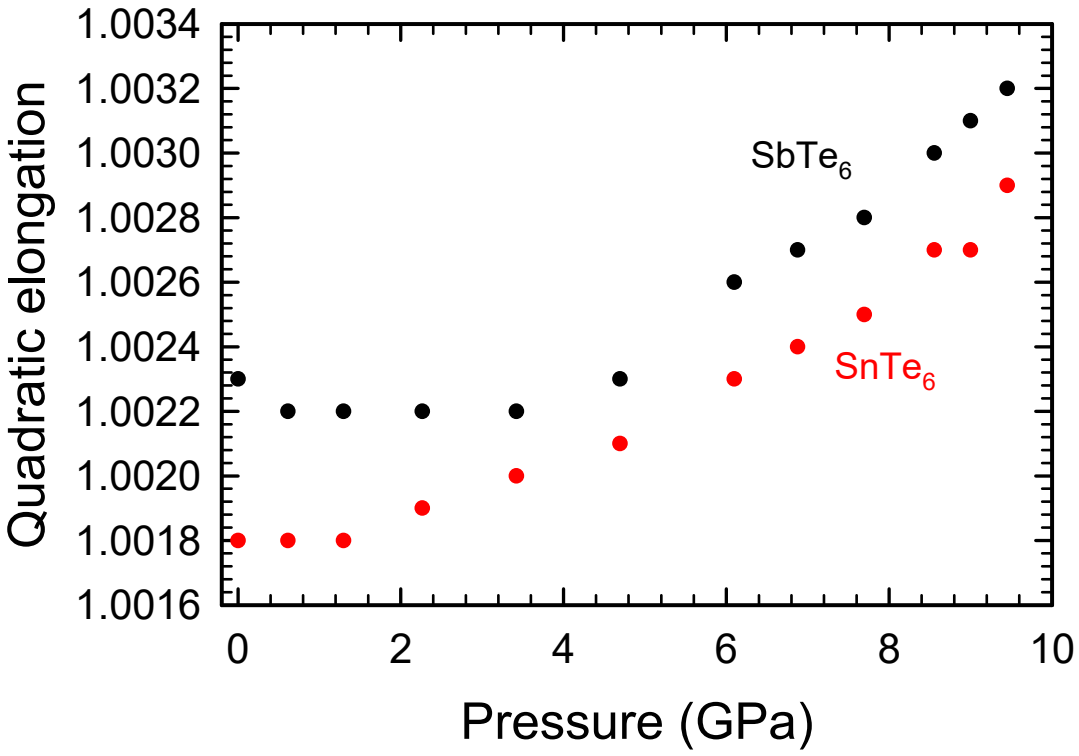

Figure S6. Pressure dependence of the theoretical quadratic elongation in the $SbTe_6$ and $SnTe_6$ octahedral units of $SnSb_2Te_4$.

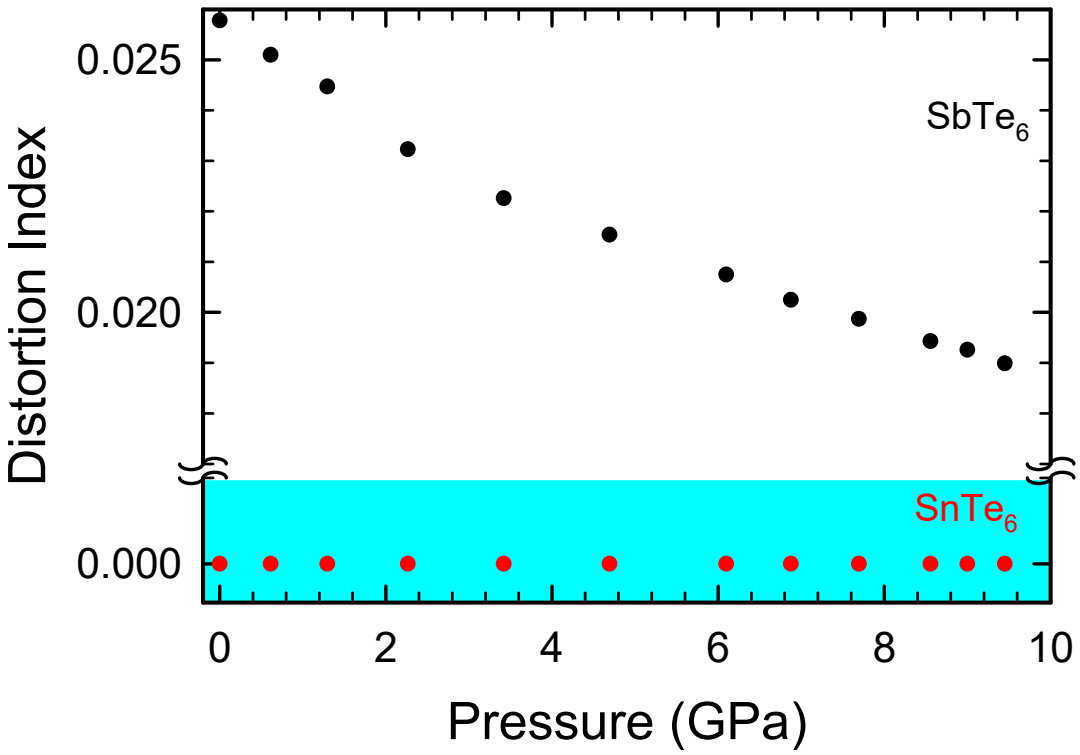

Figure S7. Pressure dependence of the theoretical distortion index of the $SbTe_6$ and $SnTe_6$ octahedral units of $SnSb_2Te_4$.

Vibrational modes in $SnSb_2Te_4$ at the Γ point

It is well-known that in layered materials, which usually crystallize either in rhombohedral, hexagonal or tetragonal space groups, the lowest-frequency E (doubly degenerated) and A (or B) modes at the Γ point can be classified as interlayer modes (low-frequency phonons mainly characterized by out-of-phase vibrations of atoms corresponding to adjacent layers) or intralayer modes (medium- and high-frequency phonons mainly characterized by out-of-phase vibrations of atoms inside the layers). Interlayer E and A (or B) modes are grouped by pairs and are usually related to shear or transversal vibrations between adjacent layers along the layer plane (*a*-*b*) and to longitudinal vibrations of one layer against the adjacent ones (along the *c* axis), respectively. These are also known as rigid layer modes and both E and A (or B) interlayer modes arises from transversal acoustic (TA) and longitudinal acoustic (LA) modes, respectively, due to the folding of the Brillouin-zone (BZ) border into the Γ-point due to the decreasing symmetry from cubic to hexagonal or tetragonal. Similarly, E and A (or B) intralayer modes come from transversal optic (TO) and longitudinal optic (LO) modes at Γ and from additional modes due to the folding of the BZ border into the Γ−point.

The number of interlayer and intralayer modes in layered materials depends on the complexity of the unit cell. In the simplest case, there should be two interlayer modes (one of E symmetry and one A or B symmetry) and two intralayer modes, such as what occurs SnS_2 **[S6]**. In the case of $SnSb_2Te_4$, there are two almost pure interlayer modes (E_g^1 and A_{1g}^1), which have the lowest frequencies and are Raman-active and correspond to out-of-phase movements of the neighbor layers both along the *a*-*b* plane (E_g^1 mode) and along *c* axis (A_{1g}^1 mode). Similar to other Raman-active modes, these modes are characterized by the immobility of the central Sn atom located in a highly symmetric Wyckoff site, the in-phase movements of all atoms of each sublayer above and below the central Sn plane and the out-of-phase movement of the atoms in the two sublayers (see **Fig. S8**). Furthermore, it can be observed that both the frequency and pressure coefficients of the interlayer A mode is larger than that of the interlayer E mode as what typically occurs in van der Waals-type layered compounds (see **Tables S1 and S2 and Figs. 6 and S19**).

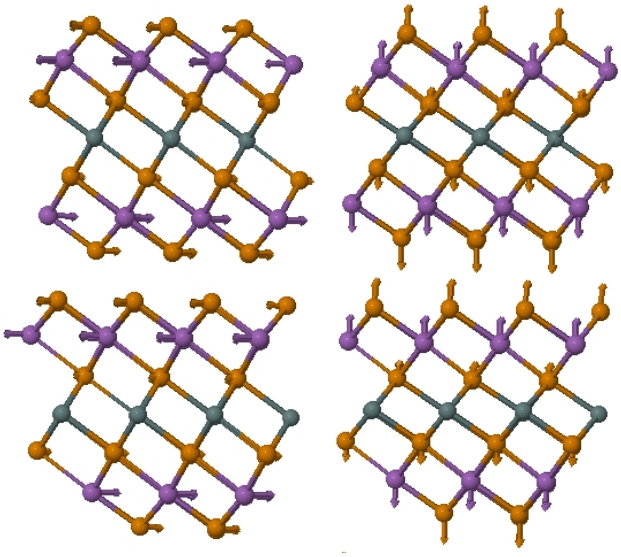

Figure S8. Atomic movements (see arrows) of low-frequency interlayer Raman-active modes E_g^1 (left) and A_{1g}^1 (right) located near 38 and 55 cm^{-1} at room pressure, respectively. Sn, Sb and Te atoms are depicted in green, purple and orange colors, respectively.

The next couple of E and A modes, discussed in order of increasing frequency, is formed by the low-frequency E_u^1 mode and the A_{2u}^1 mode (see **Fig. S9**). These two intralayer modes are characterized by an out-of-phase vibration of the central Sn atoms and the external Sb atoms. The E_u^1 mode is characterized by a vibration of the central $SnTe_6$ unit against the external $SbTe_3$ units in the a-b plane. The A_u^1 mode is the complementary mode to the E_u^1 mode and it is characterized by an out-of-phase vibration of the central $SnTe_6$ unit against the external $SbTe_3$ units along the *c*-axis.

We may observe that while all A_{2u} and E_u modes show an in-phase vibration of the neighbor Te atoms on adjacent layers, all A_{1g} and E_g modes evidence out-of-phase vibrations of neighbor Te atoms on adjacent layers similar to those modes of the pure interlayer modes. Note, however, that the intralayer modes are clearly dominated by the strong vibration amplitudes of intralayer structures. Similarly, it can be observed that the vibration of the central Sn atom is observed in all ungerade (IR-active) modes, whereas the Sn atom is mainly static in characterized by the gerade (Raman-active) modes.

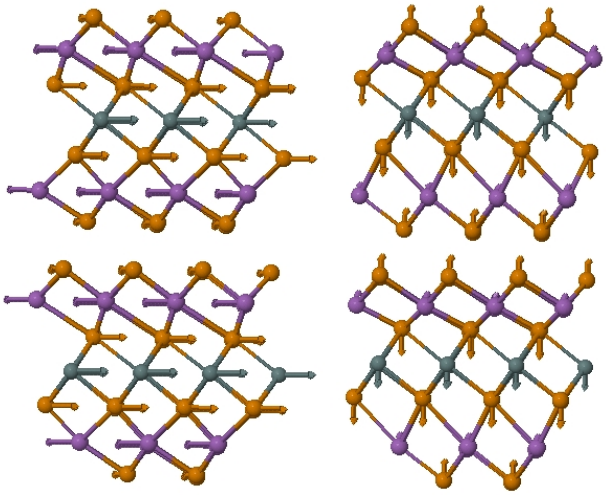

Figure S9. Atomic movements of IR-active modes E_u^1 (left) and A_{2u}^1 (right) located near 62 and 81 cm^{-1} at room pressure, respectively. Sn, Sb and Te atoms are depicted in green, purple and orange colors, respectively.

The following couple of E and A modes, in order of increasing frequency, is formed by the low-frequency E_u^2 mode and the middle-frequency A_{2u}^2 mode (see **Fig. S10**). These two intralayer modes are characterized by an in-phase vibration of the central Sn atoms and the external Sb atoms against the Te atoms. The E_u^2 mode is characterized by the vibration of the network of Sn and Sb atoms against the network of Te atoms along the a-b plane; i.e., it is the main asymmetric bending mode of the Sn-Te bond in the central $SnTe_6$ unit. On the other hand, the A_{2u}^2 mode is the complementary mode to the E_u^2 mode and it is characterized by an in-phase vibration of the central Sn atom and the Sb atoms against the network of Te atoms along the *c*-axis; i.e., it is the main asymmetric stretching mode of the Sn-Te bond in the central $SnTe_6$ unit. Therefore, these two modes are characteristic of the $SnTe_6$ octahedron and do not occur in Sb_2Te_3 as we will comment later.

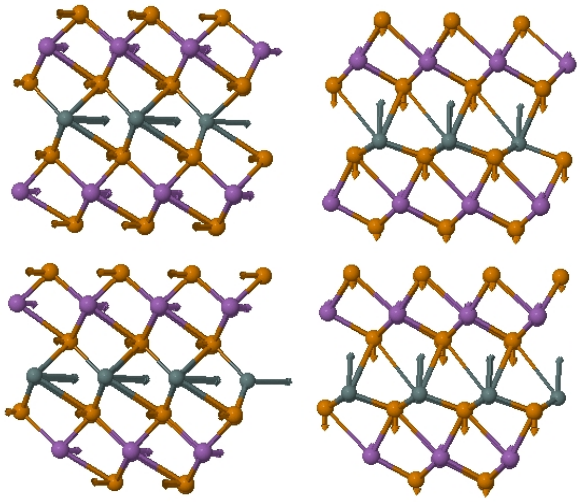

Figure S10. Atomic movements of IR-active mode E_u^2 (left) and A_{2u}^2 (right) located near 65 and 104 cm^{-1} at room pressure, respectively. Sn, Sb and Te atoms are depicted in green, purple and orange colors, respectively.

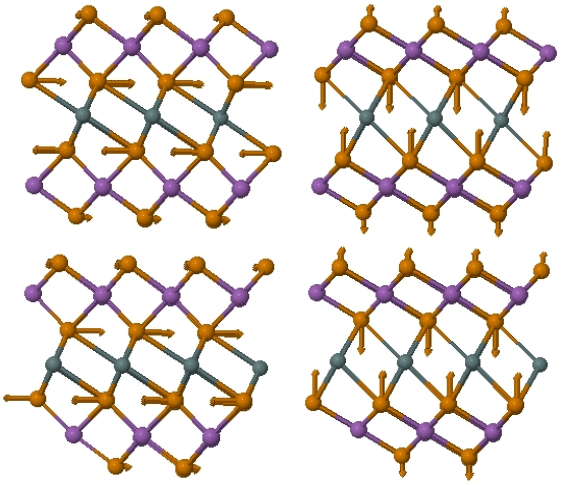

Figure S11. Atomic movements of middle-frequency Raman-active modes E_g^2 (left) and A_{1g}^2 (right) located near 100 and 115 cm^{-1} at room pressure, respectively. Sn, Sb and Te atoms are depicted in green, purple and orange colors, respectively.

The next two modes, discussed in order of increasing frequency, is formed by the medium-frequency E_g^2 and A_{1g}^2 modes (see **Fig. S11**). The E_g^2 mode is characterized by the strong out-of-phase vibration of the Te atoms close to the central Sn atoms along the a-b plane; i.e., it is the main symmetric bending mode of the Sn-Te of the central $SnTe_6$ unit. The A_{1g}^2 mode is the complementary mode to the E_g^2 and it is characterized by the strong vibration of Te atoms against Sn and Sb atoms alternately along the c axis; i.e., it

is the main symmetric stretching mode of the Sn-Te bond in the central $SnTe_6$ unit. Again, these two modes are characteristic of the $SnTe_6$ octahedron and do not occur in Sb_2Te_3 as we will comment further on.

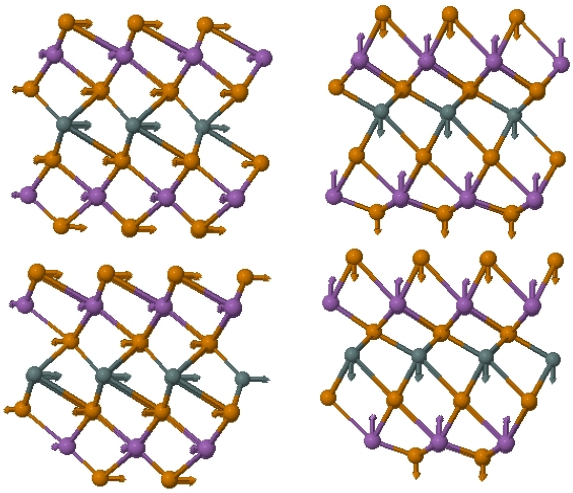

Figure S12. Atomic movements of IR-active modes E_u^3 (left) and A_u^3 (right) located near 112 and 157 cm^{-1} at room pressure, respectively. Sn, Sb and Te atoms are depicted in green, purple and orange colors, respectively.

The next pair of frequencies are formed by the medium-frequency E_u^3 mode and the high-frequency A_u^3 mode (see **Fig. S12**). These two intralayer modes are characterized by an out-of-phase vibration of the central Sn atoms and the external Sb atoms as in the E_u^1 and A_u^1 modes. Regarding the E_u^1 mode, the central Te atoms show an in-phase vibration with the central Sn atom leading to a vibration of the central $SnTe_6$ unit against the external $SbTe_3$ units in the a-b plane; however, for the E_u^3 mode the central Sn atom shows an out-of-phase vibration with respect to the adjacent Te atoms as what occurs for a Sn-Te bending mode of the $SnTe_6$ unit. Additionally, since the external Te atoms vibrate out-of-phase with respect to the Sb atoms, such a vibrational mode results also in a symmetric Sb-Te bending mode of the $SbTe_6$ unit. Similarly, the A_u^1 mode is an out-of-phase vibration of the central $SnTe_6$ unit against the external $SbTe_3$ units along the c axis; however, the A_u^3 mode corresponds solely to the central Sn atom that vibrates against the external Sb atoms in an asymmetric way (central Te atoms are static), thus leading to a coupled asymmetric Sn-Te and Sb-Te stretching mode of both $SnTe_6$ and $SbTe_6$ units.

Finally, the last two intralayer modes, referenced in order of increasing frequency is formed by the medium-frequency E_g^3 mode and the high-frequency A_g^3 mode (see **Fig. S13**). Both the E_g^3 and A_g^3 modes are characterized by the small vibration of the central $SnTe_6$ unit, such as what occurs for the E_g^1 and A_g^1 modes; however, for the E_g^1 and A_g^1 modes, the Sb atoms vibrate in phase with adjacent Te atoms, whereas in the E_g^3 and A_g^3 modes, external Te and Sb atoms move out-of-phase. Additionally, for both four modes there is an out-of-phase movement of all atoms in the two sublayers. In this way, atomic movements of Te and Sb atoms along the a-b plane evidence the E_g^3 mode as being the asymmetric bending mode of Sb-Te in the $SbTe_6$ units. Alternatively, the complementary A_g^3 mode shows Te and Sb atoms moving out-of-phase along the c axis, therefore this mode can be viewed as the asymmetric stretching mode of Sb-Te of the $SbTe_6$ units.

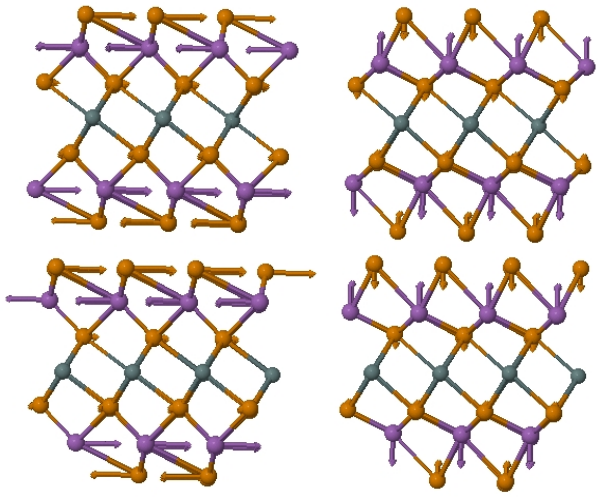

Figure S13. Atomic movements of Raman-active modes E_g^3 and A_g^3 located near 117 and 167 cm^{-1} at room pressure, respectively. Sn, Sb and Te atoms are depicted in green, purple and orange colors, respectively.

A first comparison can be stablished between the vibrational modes at Γ in $SnSb_2Te_4$ and the parent compound Sb_2Te_3. In Sb_2Te_3 there are four Raman-active modes (E_g^1, A_{1g}^1, E_g^2 and A_{1g}^2) and four IR-active modes (E_u^1, E_u^2, A_{2u}^1 and A_{2u}^2) and referenced in order of increasing frequency **[S4,S7]**. As regards to the Raman-active modes, the interlayer modes of Sb_2Te_3 are the E_g^1 and A_{1g}^1 modes (**Fig. S14**) and these are similar to the E_g^1 and A_g^1 modes of $SnSb_2Te_4$ (**Fig. S8**). For all these modes the central part of the layer remains almost static and the external adjacent Sb and Te atoms in a sublayer vibrate in-phase and also out-of-phase with respect to the atoms of the other adjacent sublayer. Similarly, the intralayer E_g^2 and A_{1g}^2 modes of Sb_2Te_3 (**Fig. S15**) are similar to the

intralayer E_g^3 and A_g^3 modes of $SnSb_2Te_4$ (**Fig. S13**) since for all these modes the central part of the layer remains almost static and the external adjacent Sb and Te atoms in a sublayer vibrate, among them and with respect to atoms of the other sublayer, out-of-phase. The similarity of E_g^2 and A_{1g}^2 modes in Sb_2Te_3 and E_g^3 and A_g^3 modes in $SnSb_2Te_4$ is so remarkable that these modes possess practically the same theoretically predicted frequency values (see **Table 3**). With respect to the Raman-active E_g^2 and A_g^2 modes of $SnSb_2Te_4$ (**Fig. S11**), these have no analog on Sb_2Te_3 since both modes involve out-of-phase vibrations of the internal Te atoms, which cannot occur in Sb_2Te_3 with only one internal Te atom.

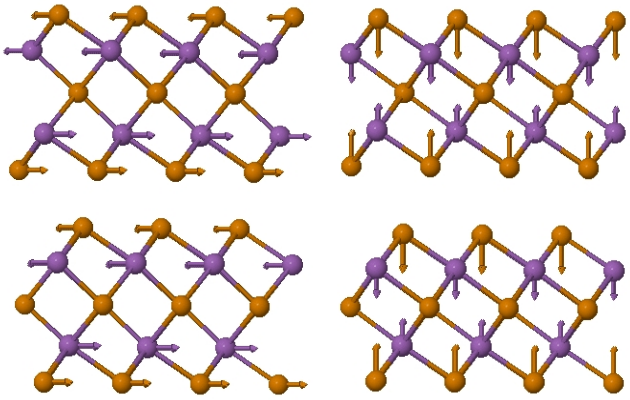

Figure S14. Atomic movements (see arrows) of low-frequency interlayer Raman-active modes E_g^1 and A_{1g}^1 in Sb_2Te_3 located near 50.4 and 68.9 cm^{-1} at room pressure, respectively. Sb and Te atoms are depicted in purple and orange colors, respectively.

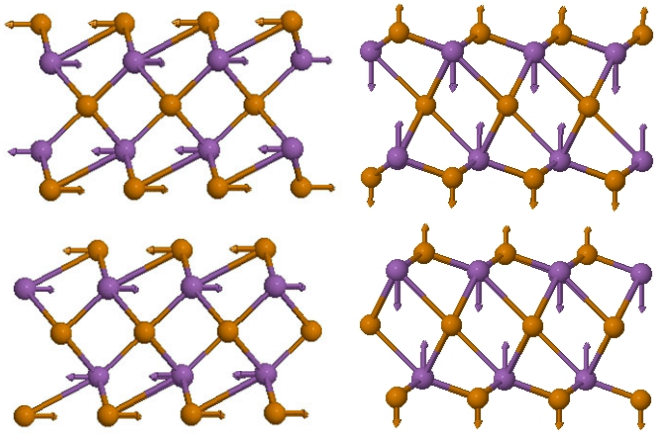

Figure S15. Atomic movements (see arrows) of high-frequency intralayer Raman-active modes E_g^2 and A_{1g}^2 in Sb_2Te_3 located near 116.6 and 167.6 cm^{-1} at room pressure, respectively. Sb and Te atoms are depicted in purple and orange colors, respectively.

With respect to the IR-active modes, the E_u^1 ($E_u(2)$ in **[S7]**) and A_{2u}^2 ($A_{2u}(3)$ in **[S7]**) modes of Sb_2Te_3 are similar to the E_u^2 and A_u^2 modes of $SnSb_2Te_4$. For both modes

of Sb_2Te_3, Sb atoms vibrate in-phase in the two sublayers and vibrate out-of-phase with respect to all Te atoms as what occurs for the E_u^2 and A_u^2 modes of $SnSb_2Te_4$. Note that the movement of the central Te atoms of the A_{2u}^2 mode is very low (not shown in **Fig. S16**) but in phase with the other Te atoms, similar to the A_u^2 mode of $SnSb_2Te_4$. On the other hand, the E_u^2 ($E_u(3)$ in **[S7]**) and A_{2u}^1 ($A_{2u}(2)$ in **[S7]**) modes of Sb_2Te_3 are similar to the E_u^3 and A_u^3 modes of $SnSb_2Te_4$. For both E_u^2 and A_{2u}^1 modes of Sb_2Te_3 central Te atoms vibrate out-of-phase with respect to the external Te atoms as to what is observed for the E_u^3 and A_u^3 modes of $SnSb_2Te_4$.

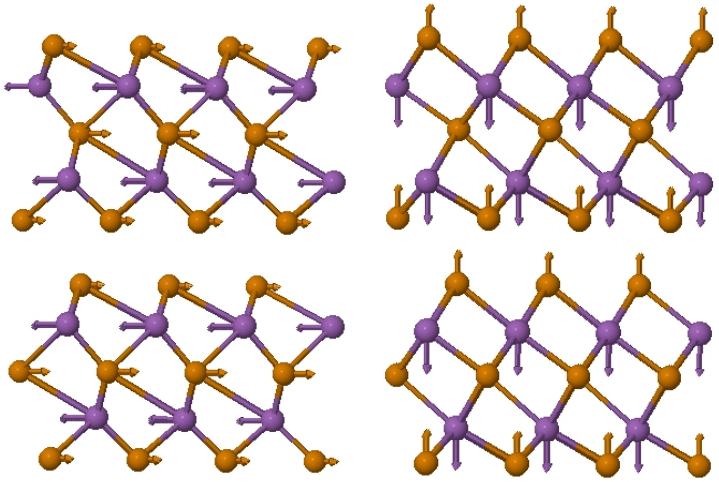

Figure S16. Atomic movements (see arrows) of intralayer IR-active modes E_u^1 and A_{2u}^2 in Sb_2Te_3 located near 78.0 and 138.7 cm^{-1} at room pressure, respectively. Sb and Te atoms are depicted in purple and orange colors, respectively.

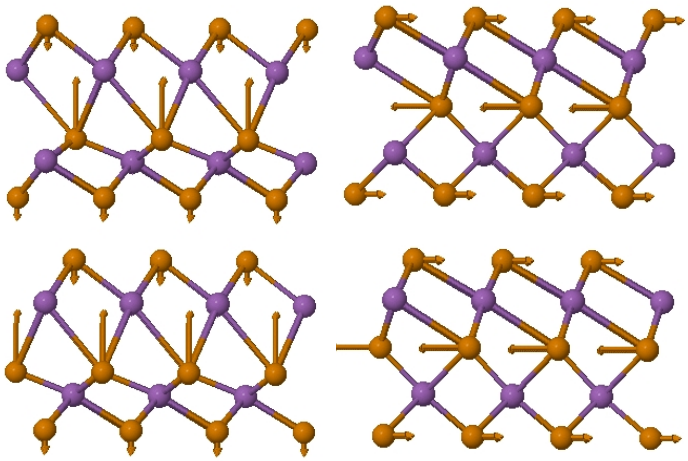

Figure S17. Atomic movements (see arrows) of intralayer IR-active modes E_u^2 and A_{2u}^1 in Sb_2Te_3 located near 100.4 and 109.9 cm^{-1} at room pressure, respectively. Sb and Te atoms are depicted in purple and orange colors, respectively.

Finally, it is noteworthy of mentioning that the IR-active E_u^1 and A_u^1 modes of $SnSb_2Te_4$ have no resemblance with IR-active modes in Sb_2Te_3. Note that these two

modes refer to the Sb atoms vibrating in-phase with their adjacent external Te atoms, a feature that does not occur in any of the IR-active modes of Sb_2Te_3. Finally, it must be stressed that for all IR-active modes of Sb_2Te_3, Sb atoms of the two sublayers vibrate in-phase, while for all Raman-active modes of Sb_2Te_3 vibrate out-of-phase. The same behavior is observed in $SnSb_2Te_4$. This is the main characteristic to discern between Raman-active and IR-active modes of both compounds.

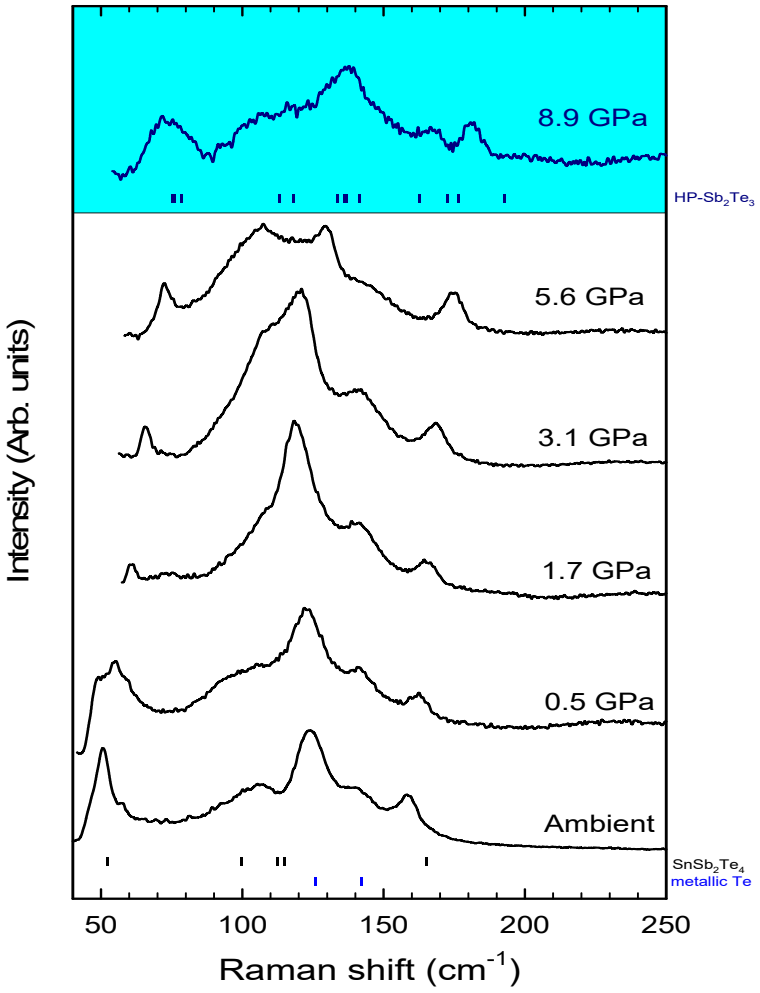

Figure S18. Raman scattering spectra of rhombohedral $SnSb_2Te_4$ at different pressures up to 8.9 GPa. Black (blue) vertical ticks correspond to theoretically predicted Raman-active mode frequency of $SnSb_2Te_4$ (Metallic Te).

Referring to the pressure coefficients of the different Raman-active and IR-active modes, it can be observed that generally the A modes have larger pressure coefficients

than their associated E modes, as it is expected in non-polar layered compounds with van der Waals forces between their layers (see **Tables S1 and S2**). This has been already commented for interlayer Raman-active E_g^1 and A_{2g}^1 modes and it applies to both $SnSb_2Te_4$ and Sb_2Te_3. Usually, the small pressure coefficient of the low-frequency E mode in layered materials is ascribed to the weak bending force constant due to weak van der Waals forces between the neighboring layers. On the other hand, the large pressure coefficient of the low-frequency A mode is due to the extraordinary increase of the stretching force constant between neighboring layers due to the strong decrease of the interlayer distance **[S4,S8]**. This behavior is also found for the low-frequency interlayer modes in layered Sb_2Te_3 and $SnSb_2Te_4$, and it is also valid for the other pairs of intralayer E and A modes, previously commented. This can be understood if intralayer E modes are mainly associated to bending Sb-Te (Sb-Te and Sn-Te) modes in Sb_2Te_3 ($SnSb_2Te_4$), while intralayer A modes are mainly associated to stretching Sb-Te (Sb-Te and Sn-Te) modes in Sb_2Te_3 ($SnSb_2Te_4$). This reasoning allows also to explain the reason for which the A modes always possess larger frequencies than their associated E modes.

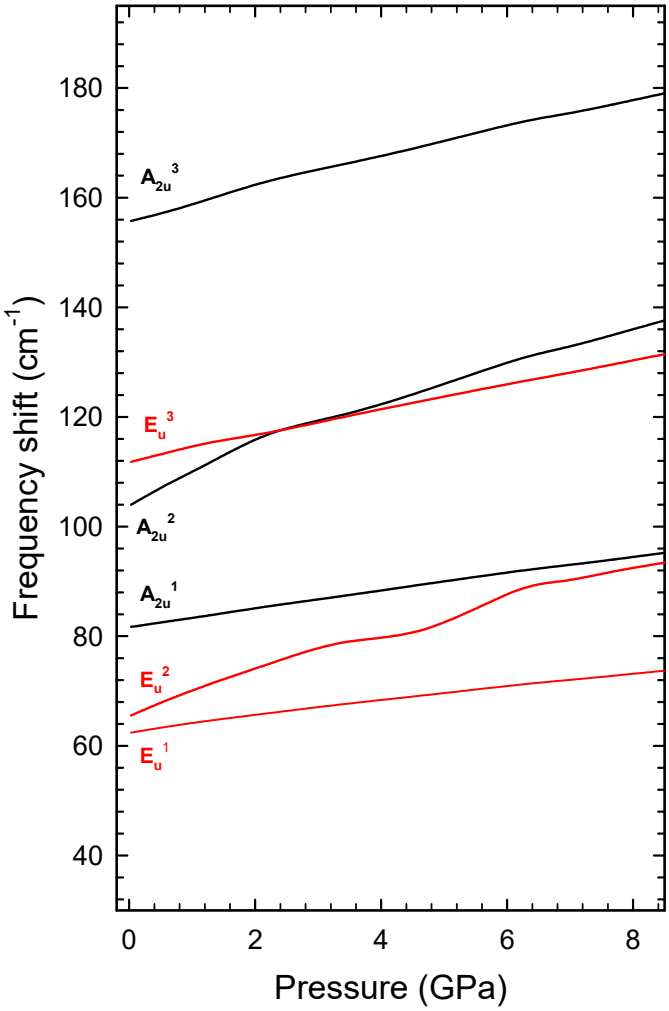

Figure S19. Pressure dependence of the theoretical IR-active modes of $SnSb_2Te_4$. A modes and doubly-degenerate E modes are depicted in black and red, respectively.

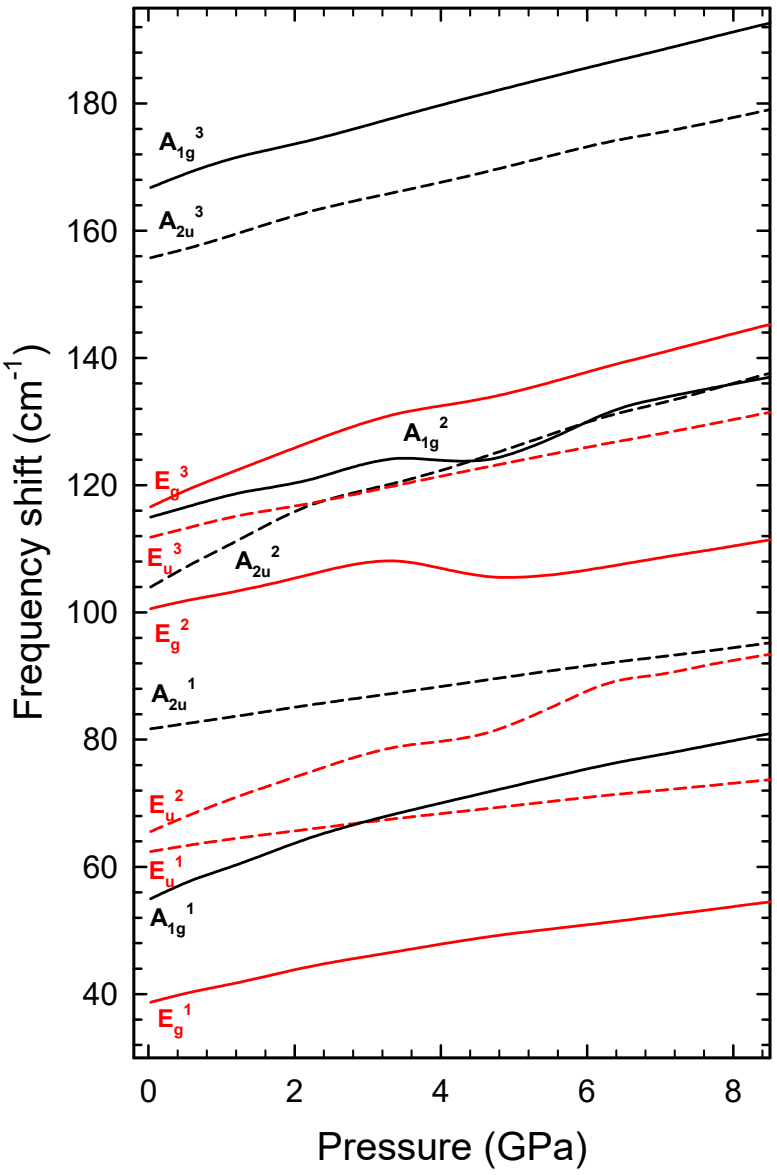

Figure S20. Pressure dependence of the theoretical (solid lines) Raman-active and (dashed lines) infrared-active mode frequencies of $SnSb_2Te_4$.

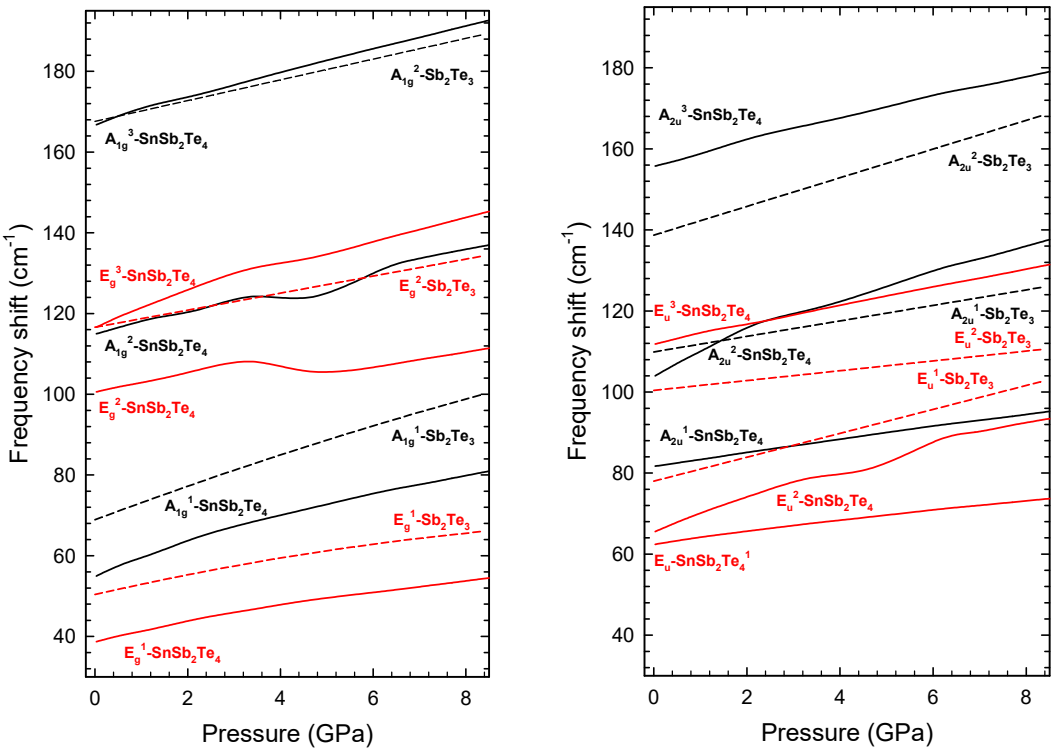

Figure S21. Pressure dependence of the theoretical (left) Raman-active and (right) infrared-active mode frequencies of $SnSb_2Te_4$ and Sb_2Te_3.

The most notable deviation of the rule mentioned above of the Raman-active modes, is that of the E_g^3 mode in $SnSb_2Te_4$. The theoretical pressure coefficient of this mode is larger than its associated A_{2g}^3 mode. This feature contrasts with Sb_2Te_3 where the equivalent modes E_g^2 and A_{2g}^2 show a normal behavior. Additionally, it must be noted that the pressure coefficient at zero pressure obtained for the A_{2g}^2 mode in $SnSb_2Te_4$ is quite high because the fit has been performed with high-pressure data due to the lack of values near room pressure.

The larger pressure coefficient of the A modes when compared to their corresponding E modes also applies for IR-active modes. Note that in Sb_2Te_3 the pressure coefficient of E_u^1 mode is smaller than its associated A_{2u}^2 mode and that of the E_u^2 mode is smaller than its associated A_{2u}^1 mode. This reasoning also applies to their similar IR-active modes in $SnSb_2Te_4$; i.e., the E_u^2 and A_{2u}^2 and the E_u^3 and A_{2u}^3 modes, respectively. Moreover, the same rule applies to E_u^1 and A_{2u}^1 modes in $SnSb_2Te_4$ that have no correspondence in Sb_2Te_3. This similarity between Raman and IR modes both in Sb_2Te_3 and $SnSb_2Te_4$ remarks the strangely large pressure coefficient of the theoretical E_g^3 mode

(which is almost double from its expected value) in $SnSb_2Te_4$, since the Raman-active A_{2g}^3 mode has a similar value of the pressure coefficient than its IR-active counterpart (the A_{2u}^3 mode).

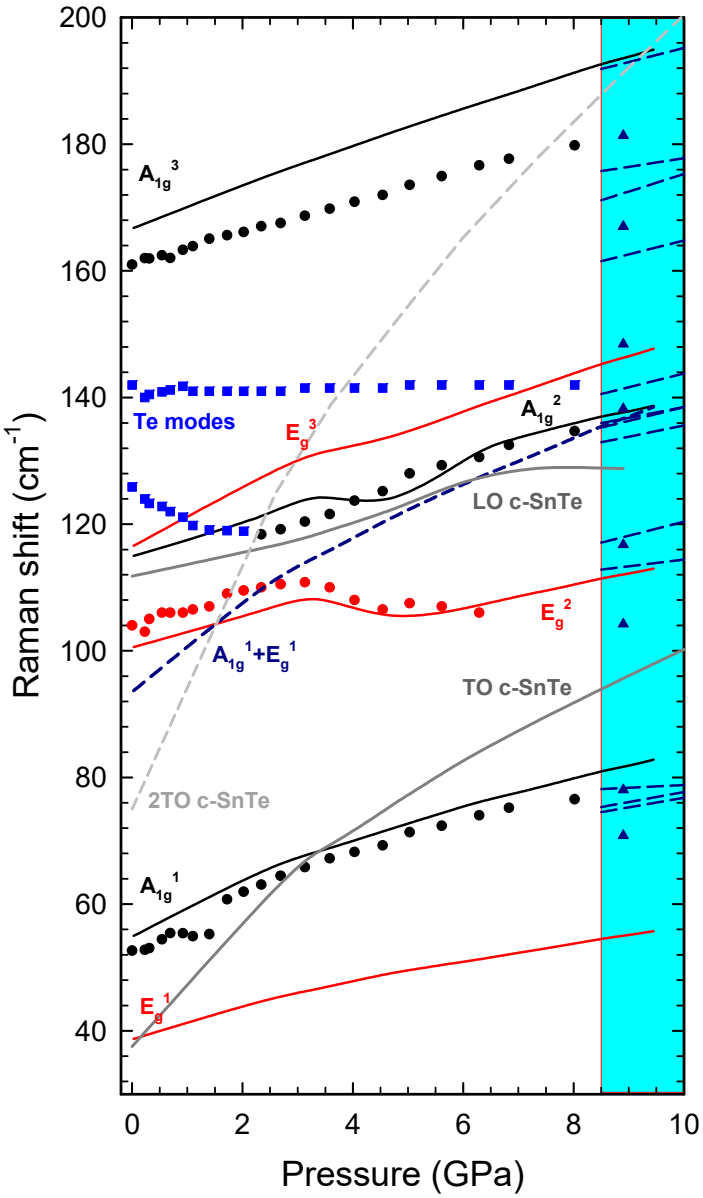

Figure S22. Pressure dependence of the experimental (symbols) and theoretical (lines) Raman-active mode frequencies in $SnSb_2Te_4$ together with the representation of theoretical LO and TO IR-active modes of c-SnTe. Dashed lines represent the pressure dependence of the $A_{1g}^1 + E_g^1$ combination at Γ in $SnSb_2Te_4$ and the 2TO mode at Γ in c-SnTe.

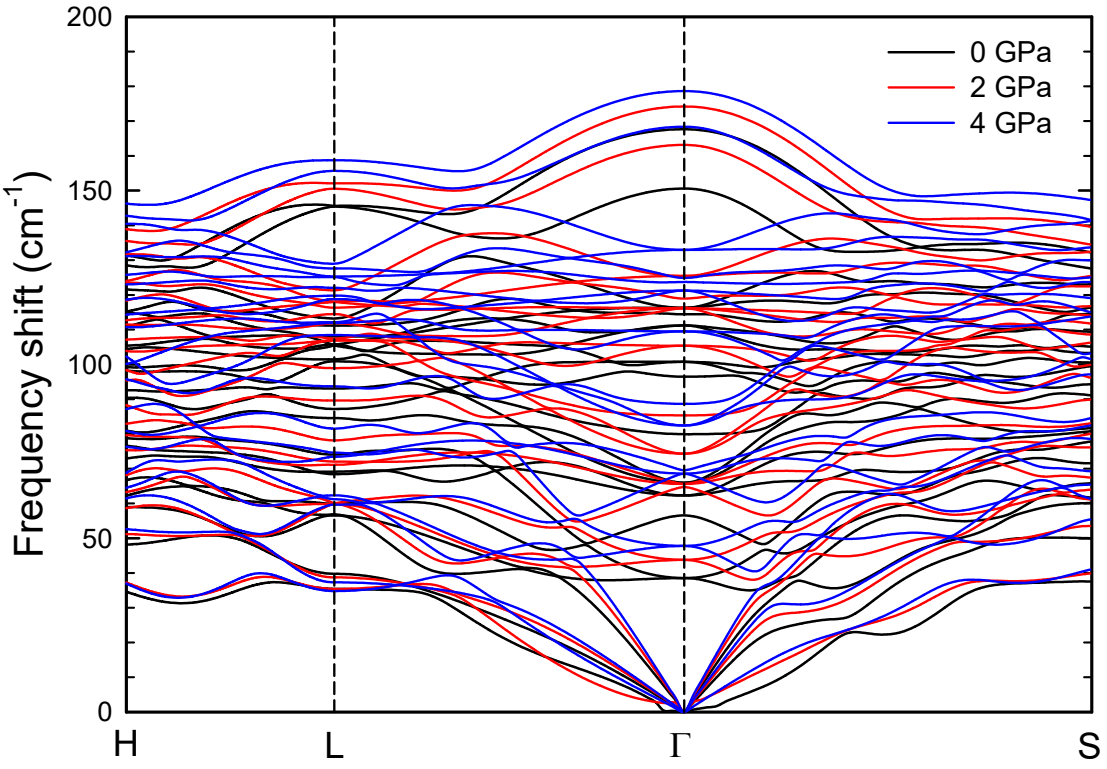

Figure S23. Phonon dispersion curves of $SnSb_2Te_4$ at 0, 2 and 4 GPa.

Evolution of the electronic topology under pressure

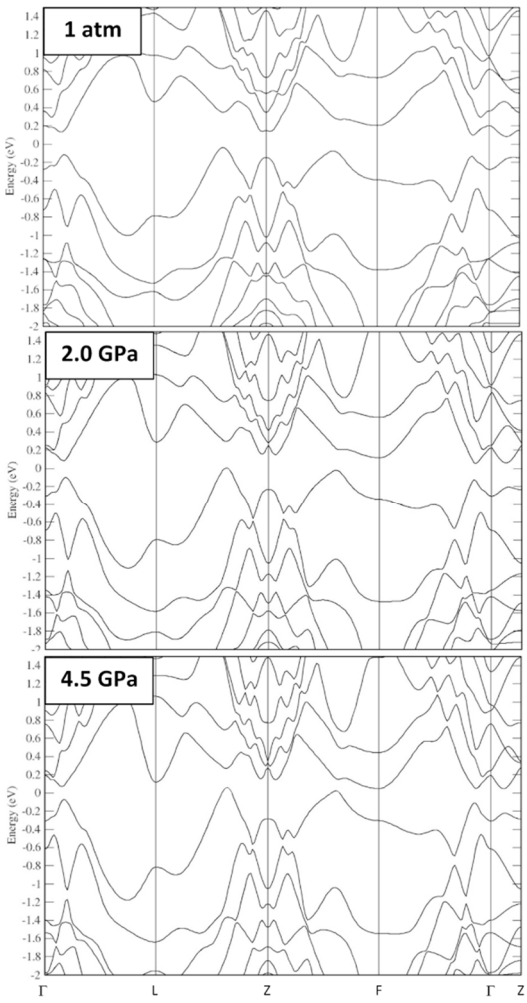

Figure S24. *Ab-initio* calculated band electronic structure of $SnSb_2Te_4$ theoretically predicted at 1 atm (top), 2 GPa (middle), and 4.5 GPa (bottom).

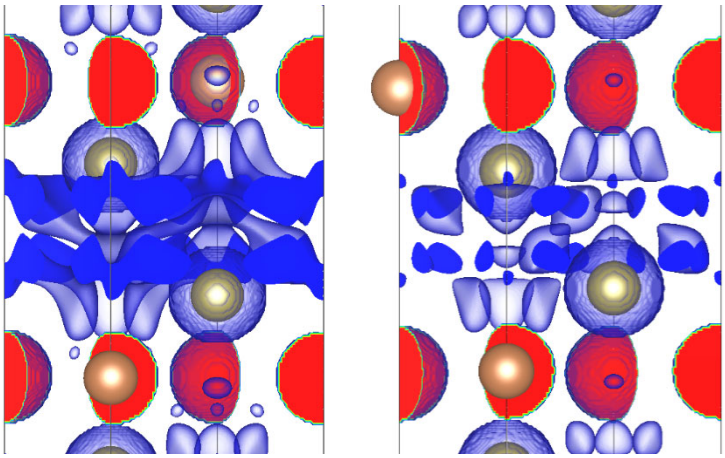

Figure S25. Reduced density gradient map of rhombohedral $SnSb_2Te_4$ around the interlayer space at 1 atm (left) and 2.5 GPa (right).

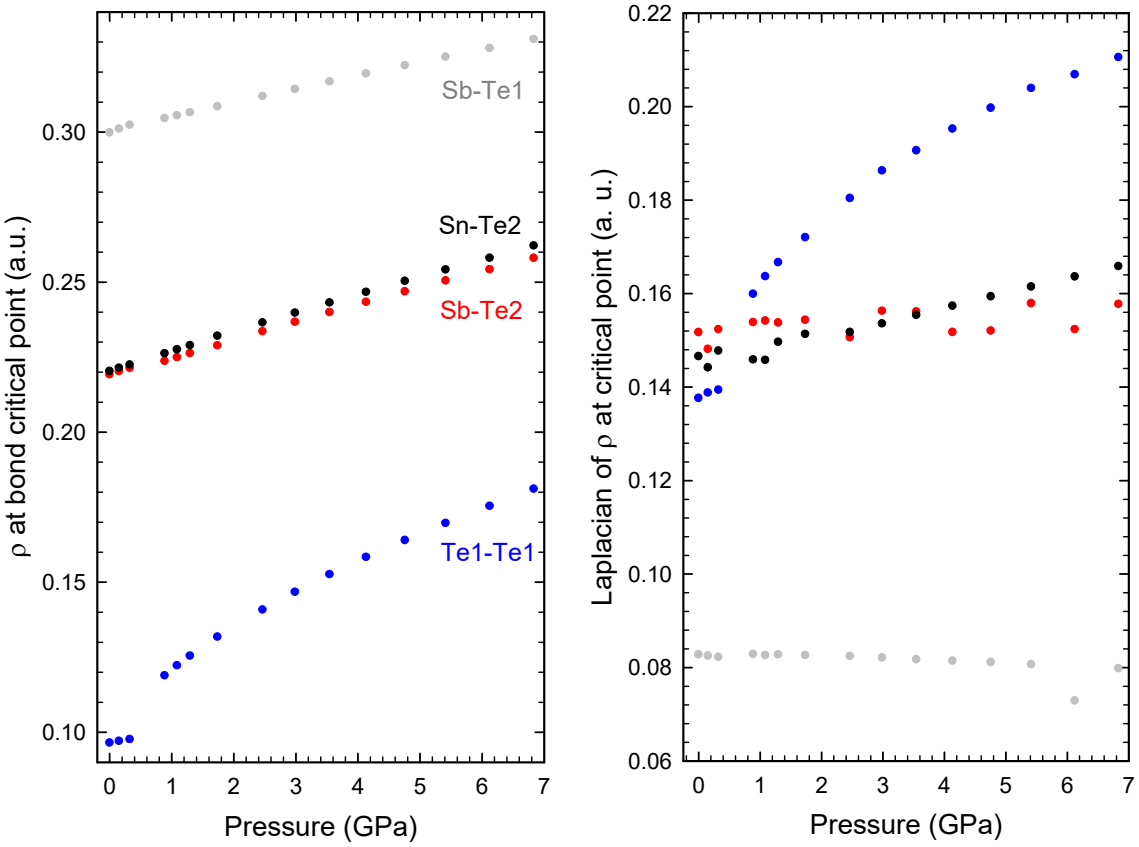

Figure S26. Pressure dependence of the electron density (left) and Laplacian of the electron density (right) at the bond critical point of the interactions of $SnSb_2Te_4$.

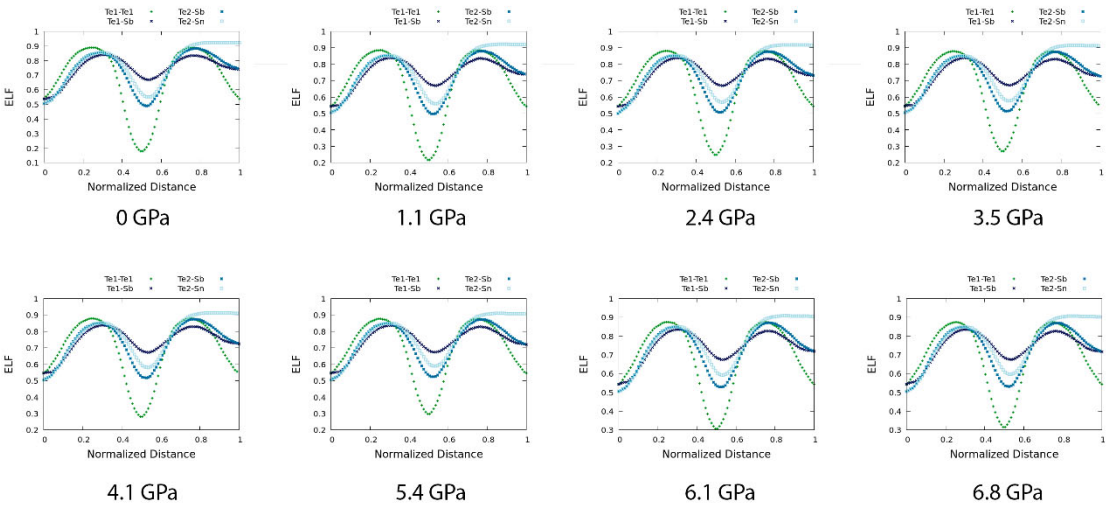

Figure S27. Pressure dependence of the ELF along the different bonds of $SnSb_2Te_4$.

Table S1. Frequencies and pressure coefficients at zero pressure of the theoretical IR-active modes in $SnSb_2Te_4$, Sb_2Te_3 and SnTe. Spin-orbit coupling has been included in all theoretical calculations.

$SnSb_2Te_4$				α-Sb_2Te_3 and c-SnTe			
Mode symmetry	**ω_0 (cm^{-1})**	**a (cm^{-1}/GPa)**	**b (cm^{-1}/GPa^2)**	**ω_0 (cm^{-1})**	**a (cm^{-1}/GPa)**	**b (cm^{-1}/GPa^2)**	**Mode symmetry**
E_u^1	62.5(5)	1.6(3)	-0.037(2)	78.0	2.9	-	E_u^1
E_u^2	65.6(2)	4.3(4)	-	100.4	1.2	-	E_u^2
A_{2u}^1	81.6(3)	1.8(2)	-0.024(2)	39.9	9.1(5)	-0.31(4)	T_{1u} (TO)
A_{2u}^2	104.0(2)	5.8(5)	-	112.9(8)	1.98(17)	-	T_{1u} (LO)
E_u^3	111.9(4)	2.5(2)	-0.021(5)	109.9	1.9	-	A_{2u}^1
A_{2u}^3	155.7(5)	3.3(7)	-0.063(7)	138.7	3.5	-	A_{2u}^2

References

[S1] B. Cordero, V. Gómez, A. E. Platero-Prats, M. Revés, J. Echevarría, E. Cremades, F. Barragán, S. Alvarez. Covalent radii revisited. *Dalton Transactions* **2008**, *21*, 2832–2838

[S2] J. E. Huheey, E. A. Keiter, R. L. Keiter. Inorganic Chemistry: Principles of Structure and Reactivity, 4th edition, HarperCollins, New York, USA, 1993.

[S3] B. A. Kuropatwa, H. Kleinke. Thermoelectric Properties of Stoichiometric Compounds in the $(SnTe)_x(Bi_2Te_3)_y$ System. Z. Anorg. Allg. Chem. **2012**, *638*, 2640-2647.

[S4] O. Gomis, R. Vilaplana, F.J. Manjón, P. Rodríguez-Hernández, E. Pérez-González, A. Muñoz, C. Drasar, and V. Kucek, Study of the lattice dynamics of Sb_2Te_3 at high pressures, Physical Review B **2011**, *84*, 174305.

[S5] D. Zhou, Q. Li, Y. Ma, Q. Cui, C. Chen. *J. Phys. Chem. C* **2013**, 117, 5352.

[S6] J.M. Skelton, L.A. Burton, A.J. Jackson, F. Oba, S.C. Parker and A. Walsh, Lattice dynamics of the tin sulphides SnS2, SnS and Sn2S3: vibrational spectra and thermal transport. Phys. Chem. Chem. Phys. **2017**, *19*, 12452.

[S7] G.C. Sosso, S. Caravati and M. Bernasconi, Vibrational properties of crystalline Sb_2Te_3 from first principles. J. Phys.: Condens. Matter **2009**, *21*, 095410.

[S8] A. M. Kulibekov, H. P. Olijnyk, A. Jephcoat, Z. Y. Salaeva, S. Onari, K. R. Allakverdiev. Raman Scattering under Pressure and the Phase Transition in ε-GaSe Phys. Stat. Sol (b) **2003**, *235*, 517-520.